Dislocation nucleation in the phase-field crystal model

Vidar Skogvoll,[1] Audun Skaugen,[2] Luiza Angheluta,[1] and Jorge Viñals[3]
[1]*PoreLab, The Njord Centre, Department of Physics, University of Oslo, P.O. Box 1048, 0316 Oslo, Norway*
[2]*Computational Physics Laboratory, Tampere University, P.O. Box 692, 33014 Tampere, Finland*
[3]*School of Physics and Astronomy, University of Minnesota, Twin Cities, Minneapolis, Minnesota 55455, USA*

(Received 16 September 2020; revised 17 November 2020; accepted 17 December 2020; published 12 January 2021)

We use the phase-field crystal model to study nucleation of edge dislocations in two dimensions under an applied stress field. A dislocation dipole nucleates under the applied stress, consistent with Burgers vector conservation. The phase field correctly accounts for elastic energy storage prior to nucleation and for dissipative relaxation during the nucleation event. We show that a lattice incompatibility field is a sensitive diagnostic of the location of the nucleation event and of the Burgers vector and slip direction of the dislocations that will be nucleated above threshold. A direct calculation of the phase-field energy accurately correlates with the nucleation event, as signaled by the lattice incompatibility field. We show that a Schmid-like criterion concerning the resolved stress at the nucleation site correctly predicts the critical nucleation stress. Finally, we present preliminary results for a three-dimensional, bcc lattice. The phase field allows direct computation of the lattice incompatibility tensor for both dislocation lines and loops.

DOI: 10.1103/PhysRevB.103.014107

I. INTRODUCTION

Unlike the spontaneous homogeneous nucleation of topological defects in a symmetry-breaking phase transition [1–3], the formation of dislocation lines in a material is typically studied as an athermal process largely driven by local stresses [4]. Since the existence and mobility of such defects are essential contributors to the strength and ductility of crystalline materials, understanding the mechanisms behind their creation and motion is a fundamental goal of material science in general and of plasticity theory in particular. Along parallel developments in the continuum theory of crystal plasticity, a number of empirical criteria have been introduced to predict dislocation nucleation thresholds, the resulting Burgers vector distribution, and line direction [5–8]. These macroscopic criteria have been extensively compared with microscopic results from molecular dynamics (MD) simulations of model crystalline solids in a variety of configurations and imposed stresses [8–11]. However, the details of the mechanical conditions that lead to dislocation nucleation still remain poorly understood, with criteria from continuum mechanics approaches and numerical simulations often yielding conflicting phenomenology. The two main reasons why a precise comparison between the two is difficult include the disparity in length scales between crystal plasticity theory and molecular simulation and the necessity in the latter to thermally average phase space trajectories that take place over characteristic energy scales which are much higher than thermal scales. Fundamental questions such as whether the nucleation event is local or nonlocal remain unresolved [8]. We bridge here microscopic and continuum scales by introducing a phase-field crystal model [12,13] of dislocation nucleation and show that the nucleation event is well captured at the mesoscale by a continuum lattice incompatibility field. Our numerical results for the nucleation of edge dislocations in a two-dimensional (2D), hexagonal lattice indicate that the nucleation event is governed by a local balance between the resolved stresses along lattice slip planes and the force acting between the nucleating dislocation pair and that a lattice incompatibility field derived from the phase field predicts the Burgers vector of the nucleating defect pair. The simplest dislocation nucleation criterion is based on the Schmid stress decomposition [5,7,14–17]. When an appropriate projection of an atomic level shear stress exceeds a material-dependent threshold, a dislocation loop is predicted to be nucleated. On the one hand, while fcc lattices generally obey the Schmid criterion, there exist entire classes on "non-Schmid" lattices, including bcc crystals [18]. Furthermore, a recent, careful MD study of nucleation in a nanoindentation configuration for a model Lennard-Jones solid shows that the Schmid criterion not only fails to account for the site of the nucleation event but nucleation, in fact, occurs in regions in which the resolved shear stress is relatively small [8]. A second class of criteria associates the nucleation event to a buckling or phonon instability of the lattice (the Hill or Λ criteria based on mechanical stability arguments [7,16]). Molecular dynamics simulations and experiments in different crystal indentation configurations, however, have revealed very complex nucleation processes in which the lattice is locally quite distorted and therefore far from the conditions of applicability of such a phonon stability analysis. Large regions of partial dislocations and extended stacking faults have been argued to be present at nucleation [9], as well as extended and complex networks involving surfaces and grain boundaries [11]. More recently, the stability of the perfect lattice against homogeneous nucleation was formulated in terms of the kinematic equation that governs the temporal evolution

of the dislocation density tensor. This approach is sensitive to the creation of nontrivial local topology [8] and yields predictions that are qualitatively different than the Schmid criterion. To contribute to the elucidation of the criteria for nucleation, we examine here a simple, prototypical configuration: a 2D hexagonal lattice in which nucleation occurs through the formation of a dislocation dipole of zero net Burgers vector. In this idealized configuration, we show that the incompatibility field directly computed from the phase field identifies the nucleation event and that it can be used to predict the Burgers vector at nucleation. The critical stress for nucleation is seen to be in quantitative agreement with that of the Schmid criterion in this 2D lattice.

II. THE PHASE-FIELD CRYSTAL

The phase-field crystal (PFC) model is a mesoscale description of a crystalline solid in which vibrational degrees of freedom have been averaged out, in the same spirit as density functional theory [13,19]. The crystalline phase is described by a scalar order parameter field $\psi(\mathbf{r})$, which obeys a phenomenological free energy given, in dimensionless form, by

$$\mathcal{F}[\psi] = \int d\mathbf{r}\left[\frac{1}{2}[\mathcal{L}\psi]^2 + \frac{r}{2}\psi^2 + \frac{1}{4}\psi^4\right], \tag{1}$$

where $\mathcal{L} = 1 + \nabla^2$ and r is a dimensionless parameter representing the deviation from the liquid-solid phase boundary.

We further assume that ψ is a conserved variable, with its spatial average $\bar{\psi}$ being constant [19]. The two constants r and $\bar{\psi}$ completely define the model. In two dimensions, for a range of values of $\bar{\psi}$ and $r < 0$, a triangular Bravais lattice $\psi^{\mathrm{eq}}(\mathbf{r})$ is the equilibrium phase, which we consider here.

Upon deformation of the equilibrium state ψ^{eq} by a displacement field $\mathbf{u}(\mathbf{x})$, it is possible to define the equilibrium stress tensor as the variation of the free energy with respect to the displacement gradient [20],

$$\tilde{\sigma}^{\psi}_{ij} = -\partial_m[\psi\,\partial_m\mathcal{L}\psi]\delta_{ij} + 2[\partial_{(i}\mathcal{L}\psi][\partial_{j)}\psi], \tag{2}$$

where $X_{(i}Y_{j)}$ refers to symmetrization of indices i, j [21]. This quantity still shows spatial variations within a unit cell due to the variation of ψ. We therefore further define an averaged stress field as $\sigma^{\psi}_{ij} = \langle\tilde{\sigma}^{\psi}_{ij}\rangle$, where $\langle\cdot\rangle$ refers to averaging over an area approximately equal to a unit lattice cell.

For small distortions, the hexagonal lattice is elastically isotropic. We define a symmetric strain as

$$e^{\psi}_{ij} = \frac{1}{2\mu}\left(\sigma^{\psi}_{ij} - \kappa\delta_{ij}\sigma^{\psi}_{kk}\right), \tag{3}$$

where μ is the shear modulus and $\kappa = \lambda/[2(\lambda+\mu)]$, where λ is the standard Lamé coefficient. In our dimensionless variables, we have $\lambda = \mu = 3A_0^2$, where A_0 is the amplitude of ψ^{eq} [20].

Dislocations lead to lattice incompatibility [4,22]. In two dimensions and given a Burgers vector density $\mathbf{B}(\mathbf{r})$, the incompatibility field is $\eta = \epsilon_{ik}\epsilon_{jl}\partial_i e_{kl} = \epsilon_{ij}\partial_i B_j$. A key assumption of our analysis is that the configuration of ψ contains the complete strain incompatibility [23,24]. Thus, from Eq. (3) we find

$$\eta^{\psi} = \frac{1}{2\mu}\left(\epsilon_{ik}\epsilon_{jl}\partial_{ij}\sigma^{\psi}_{kl} - \kappa\nabla^2\sigma^{\psi}_{kk}\right). \tag{4}$$

The dissipative evolution of ψ is diffusive,

$$\partial_t\psi = \nabla^2\frac{\delta\mathcal{F}}{\delta\psi}, \tag{5}$$

with a constant kinetic mobility coefficient, which we set to 1 in our study and which sets the unit of time. As discussed in Refs. [23,25], lattice distortion needs to be treated separately from diffusive relaxation of ψ in order to incorporate elastic response into the phase field and to maintain elastic equilibrium at all times. In addition, in order to induce nucleation, we consider an externally imposed bulk stress $\sigma^{\mathrm{ext}}_{ij}(\mathbf{r})$. In elastic equilibrium $\partial_i\sigma^{\psi}_{ij} = \partial_i\sigma^{\mathrm{ext}}_{ij}$. Following Ref. [23], for a nonequilibrium configuration of ψ, we solve $\partial_i(\sigma^{\psi}_{ij} - \sigma^{\mathrm{ext}}_{ij} + \sigma^{\delta}_{ij}) = 0$, where $\sigma^{\delta}_{ij} = \lambda e^{\delta}_{kk} + 2\mu e^{\delta}_{ij}$ and e^{δ}_{ij} is a compatible strain, $e^{\delta}_{ij} = (\partial_i u^{\delta}_j + \partial_j u^{\delta}_i)/2$. Diffusion of ψ is supplemented at each time by distortion $\psi(\mathbf{r}) \to \psi(\mathbf{r} - \mathbf{u}^{\delta})$.

In two dimensions, the condition for elastic equilibrium means that the stress tensor difference can be written in terms of an Airy potential χ, $\sigma^{\psi}_{ij} - \sigma^{\mathrm{ext}}_{ij} + \sigma^{\delta}_{ij} = \epsilon_{ik}\epsilon_{jl}\partial_{kl}\chi$. For each instantaneous configuration of ψ we solve [23]

$$\frac{1-\kappa}{2\mu}\nabla^4\chi = \eta^{\psi} - \eta^{\mathrm{ext}}, \tag{6}$$

where η^{ext} accounts for the fact that the imposed stress does not necessarily derive from a compatible displacement. The solution allows the computation of e^{δ}_{ij} and, from it, of the displacement u^{δ}_i.

III. NUMERICAL METHOD

A square computational domain is considered with periodic boundary conditions, with 100×100 hexagonal unit cells of length $a_0 = \frac{4\pi}{\sqrt{3}}$ and grid spacings $\Delta x = a_0/7$ and $\Delta y = a_0\sqrt{3}/12$. The model parameters used are $r = -1$ and $\bar{\psi} = -0.45$. The initial condition of ψ is a periodic, undistorted hexagonal lattice. For our choice of model parameters, the corresponding Lamé coefficients are $\mu = \lambda = 0.227$.

Calibrating the parameter values to experiments is a difficult task due to a lack of high-resolution data and corresponding measurable quantities. Since the PFC free energy is an effective coarse graining of the intermolecular potential related to high-order density gradients, a substantial amount of fitting is required, beginning with energy scales, but also relaxation timescales [13]). Hence, the strength of the PFC model is not in modeling with specific dimensional units, but rather in modeling generic behavior described by rescaled units. To this end, the shear modulus μ sets the unit for measuring stress, while strain and incompatibility fields are dimensionless. For instance, the critical stress of 0.081 in Fig. 2 would correspond in physical units to $\sigma_c^* = 0.081/0.227\mu \approx 0.36\mu$.

We impose a shear stress $\sigma^{\mathrm{ext}}_{xx} = \sigma^{\mathrm{ext}}_{yy} = 0$ and $\sigma^{\mathrm{ext}}_{xy} = \sigma_0 e^{-\frac{|\mathbf{r}-\mathbf{r}_0|^2}{2w^2}}$, with $\mathbf{r}_0$ being an arbitrary center. Nucleation is induced by a sequence of steps of increasing value of σ_0.

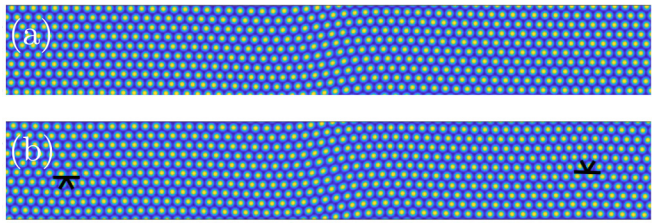

FIG. 1. Central region of the computational domain with (a) the PFC configuration in equilibrium at $\sigma_0 = 0.080$ prior to nucleation and (b) the equilibrium configuration at $\sigma_0 = 0.081$ after nucleation.

A given configuration is allowed to relax to equilibrium for constant σ_0. After equilibration has been achieved, the configuration is used as the initial condition for another relaxation step in which the value of σ_0 is increased. The details are as follows: Diffusive relaxation of ψ is allowed for 100 steps by using an exponential time differencing method, with a time step of $\Delta t = 0.1$ [26]. After these 100 steps, ψ is brought to mechanical equilibrium by a compatible displacement as described above and in Refs. [23,27]. Diffusive relaxation and elastic distortion cycles are continued until the largest change in ψ between two such cycles is less than 0.01. We then increase σ_0 by an increment $\Delta\sigma_0 = 0.001$ and repeat the relaxation procedure. The external stress amplitude considered ranges from zero to $\sigma_0 = 0.086$. Figure 1 shows the equilibrated field ψ for some amplitude of σ_0 prior to ($\sigma_0 = 0.080$) and after a nucleation event ($\sigma_0 = 0.081$) for $w = 4a_0$. The nucleation event gives rise to two edge dislocations with opposite Burgers vectors $a_0\mathbf{e}_x$ and $-a_0\mathbf{e}_x$. When the configuration comprising two defects is allowed to evolve, the defects move away from each other along the x direction. Note that since a dislocation in a hexagonal lattice has two extra half planes, we represent the location of the dislocation by the symbol $\perp\!\!\!\perp$. This is in contrast to the conventional symbol representing an edge dislocation ($\perp$), which indicates the directions of the slip and extra inserted half plane. A video animation of the nucleation event sequence can be found in the Supplemental Material [28].

IV. TWO-DIMENSIONAL DISLOCATION NUCLEATION

The incompatibility field η^ψ from Eq. (4) accurately indicates where dislocations form. Figures 2(a) and 2(b) show the η^ψ field corresponding to the ψ density field in Fig. 1, before and after the nucleation event. The extremes in the value of η^ψ identify the location of the defect cores. Also, the quadrupolar structure of Fig. 2(a) *prior* to nucleation reflects the Burgers vectors of the dislocation pair to be nucleated. More quantitatively, Fig. 2(c) shows the evolution of the maximal value of η^ψ in time and upon increasing σ_0 quasistatically (shown by the left y axis). The point at which σ_0 attains the critical value for nucleation is marked by the vertical dashed line at $t = 2050$, and the dislocations become distinct at $t \approx 2300$. We observe that $\max(\eta^\psi)$ rises before the dislocations become distinct. Prior to nucleation, the crystal lattice is elastically loaded with a quasistatic increase of σ_0. After nucleation, the external stress σ_0 remains constant (corresponding to a plateau

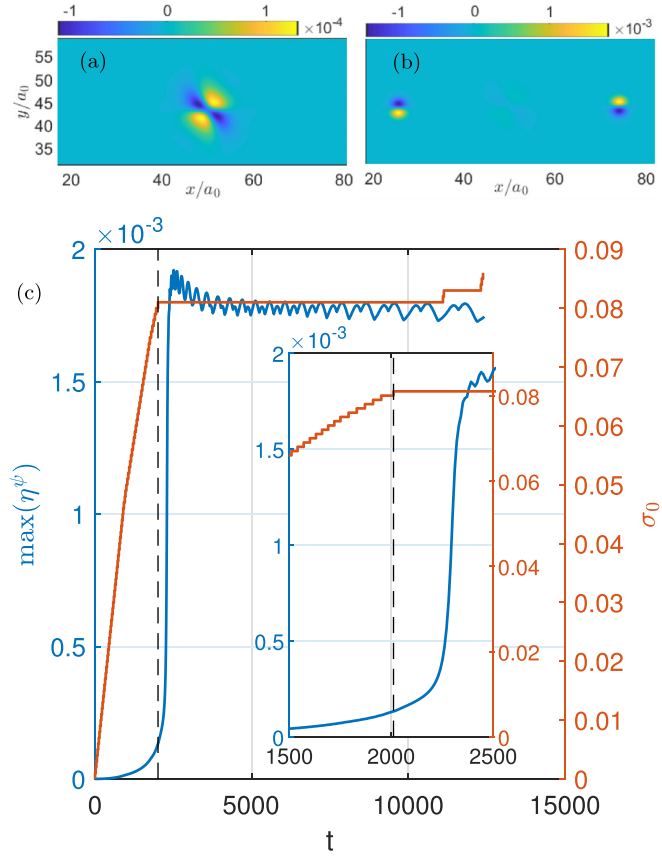

FIG. 2. Incompatibility field η^ψ (a) at $t = 2050$ ($\sigma_0 = 0.080$), before the nucleation event, and (b) at $t = 12170$ ($\sigma_0 = 0.081$), after nucleation. (c) Maximum of η^ψ as a function of time t. The dashed line at $t = 2050$ marks where σ_0 has attained the critical value for nucleation. The dislocations become distinct at $t \approx 2300$. The right axis shows the value of σ_0 for the corresponding times. The plateaus in time indicate nonequilibrium relaxation at constant external stress.

in the σ_0 curve), while the crystal lattice evolves diffusively in time.

Figure 3 further shows the corresponding change in the PFC free energy $\mathcal{F}$ upon increasing σ_0, together with the elastic energy defined as $E_{el} = \frac{1}{2}\int d\mathbf{r}\sigma_{ij}^\psi e_{ij}^\psi$. Note that despite the purely diffusive dynamics obeyed by ψ, the lattice is capable of storing (reversible) elastic energy upon increasing the value of σ_0, as seen previously in Fig. 2(c). This reversible evolution is enabled through the compatible distortion added to the field ψ to preserve elastic equilibrium. As the nucleation event is reached, the phase-field energy exhibits a large discontinuity at the value of σ_0 that corresponds to the dashed line in Fig. 2(c).

For this simple 2D setup, it is possible to predict the critical stress for nucleation from the value of the resolved shear stress along each slip plane, in analogy with the classical Schmid criterion. For a given stress σ_{ij}, the resolved shear stress $\tau_{\mathbf{a},\mathbf{n}}$ on a slip plane defined by the normal unit vector $\mathbf{n}$ along a direction in the slip plane given by the unit vector $\mathbf{a}$ is $\tau_{\mathbf{a},\mathbf{n}} = a_i\sigma_{ij}n_j$. In two dimensions, $\mathbf{n}$ is determined up to a sign by $n_i = \epsilon_{ij}a_j$, and for the hexagonal symmetry, there are three slip planes defined by lattice vectors

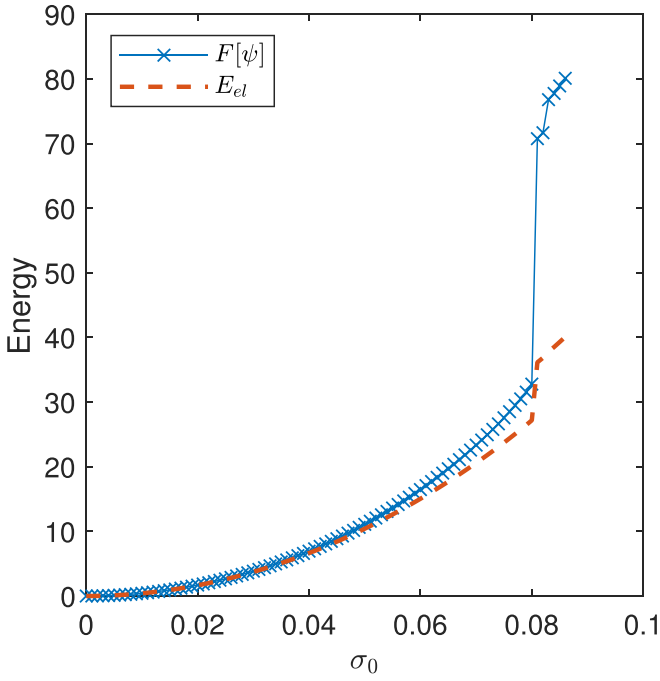

FIG. 3. Total free energy $\mathcal{F}$ and elastic energy E_{el} as a function of σ_0.

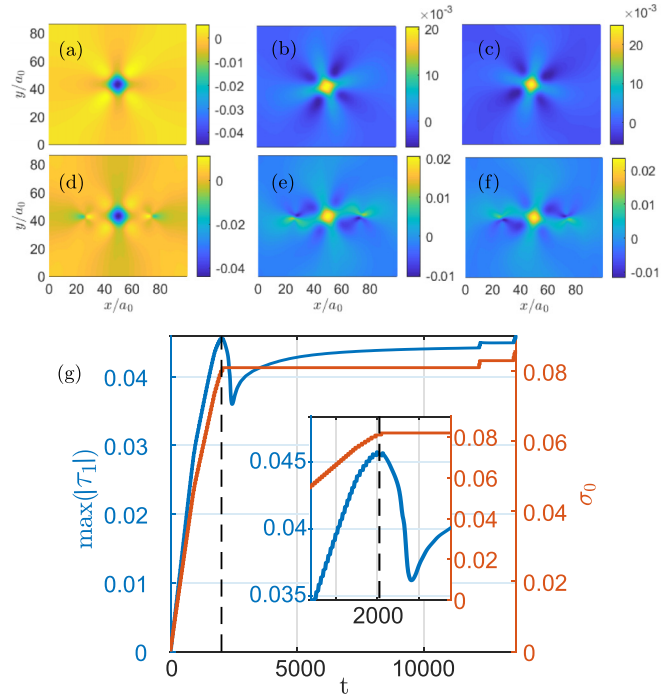

FIG. 4. The resolved shear stresses just prior to and after the nucleation event. (a)–(c) τ_1, τ_2, and τ_3 at $t = 2050$ ($\sigma_0 = 0.080$), respectively, and (d)–(f) τ_1, τ_2, and τ_3 at $t = 12170$ ($\sigma_0 = 0.081$), respectively. (g) $\max(|\tau_1|)$ as a function of time t during the nucleation event.

$\mathbf{a}_1 = [1, 0]$, $\mathbf{a}_2 = [1/2, \sqrt{3}/2]$, and $\mathbf{a}_3 = [-1/2, \sqrt{3}/2]$. One thus considers three different scalar fields τ_1, τ_2, and τ_3, which are the resolved shear stresses along the slip directions corresponding to $\mathbf{a}_1$, $\mathbf{a}_2$, and $\mathbf{a}_3$, respectively. Figures 4(a)–4(f) show the fields τ_1, τ_2, τ_3 right before and after nucleation. The resolved shear stress is largest along the $\mathbf{a}_1$ direction, the slip plane along which the dislocation pair nucleates, and is centered at the origin, the nucleation site. The other two resolved stresses remain small during nucleation. The change in the largest resolved stress τ_1 is shown in Fig. 4(g), using the same coordinates as in Fig. 2(c). Nucleation initiates (vertical dashed line) when the resolved shear stress approaches the critical value of $|\tau_c| = 0.046$, followed by a small drop and then a slow rise as the newly nucleated dislocation dipole moves away from the center region. Notice that this value of τ_c at the moment of nucleation is smaller than the external shear stress $\sigma_{xy}^{\text{ext}} = 0.080$. This is because at mechanical equilibrium, the two stresses are equal only up to a divergence-free term. The critical value of the resolved stress τ_c can be estimated as follows: Consider an otherwise perfect lattice with a bound dislocation pair of opposite Burgers vectors. The force acting on the dislocations (in opposite directions) because of the external stress is the Peach-Koehler force projected on the slip plane defined by $\mathbf{a}_k$ and is $F_k^{PK} = b\tau_k = \pm a_0\tau_k$ for dislocations with Burgers vectors $\mathbf{b} = \pm a_0\mathbf{a}_k$. As the two dislocations in the dipole separate at nucleation to become distinct, their mutual elastic interaction results in an attractive force. If both dislocations are on the x axis, this force is [29,30] $|f_x| = Y_2 b^2/(4\pi d)$, where $Y_2 = 4\mu(\lambda + \mu)/(\lambda + 2\mu)$ is the 2D Young's modulus and d is the dislocation separation. We estimate τ_c as the applied stress for which the resulting Peach-Koehler force on one dislocation equals the force from the other dislocation when the separation is one lattice constant. We find that $\tau_c = Y_2/(4\pi)$. Using the numerical values of $\mu = \lambda = 0.2271$, $Y_2/(4\pi) = 0.048$, which is in close agreement with the observed value of $|\tau_c| = 0.046$.

In order to further test the nucleation criterion, we have performed additional calculations in which the imposed stress σ_{ij}^{ext} is rotated relative to the lattice, $\sigma_{ij}^{\text{ext}}(\theta) = R_{ki}^{(\theta)}\sigma_{kl}^{\text{ext}}R_{lj}^{(\theta)}$, where $R_{ij}^{(\theta)}$ is the standard rotation matrix in two dimensions and θ is the rotation angle. Figure 5 shows the maximal resolved stress at nucleation along the three lattice directions as a function of θ. Since σ_{ij}^{ext} is invariant under a rotation of π, $\sigma_{ij}^{\text{ext}}(x) = \sigma_{ij}^{\text{ext}}(\pi + x)$, we show only values ranging from $\theta = 0$ to π. Figure 5 shows that the resolved stress consistently predicts the type of dislocation dipole to nucleate, but the value of the critical resolved stress depends on θ and is, in general, lower than $Y_2/(4\pi)$. The discrepancy is likely due to anisotropic contributions to lattice distortions at the length scale of the core which are not described by isotropic linear elasticity.

V. THREE-DIMENSIONAL INCOMPATIBILITY FIELD

The simplest example of a 2D hexagonal lattice has only point edge dislocations and is described by isotropic elasticity. However, more realistic crystal lattices have more complex loop defects and lattice anisotropy, where the Schimd-like criterion might not readily apply. Therefore, it is important to understand how the incompatibility field applies to three

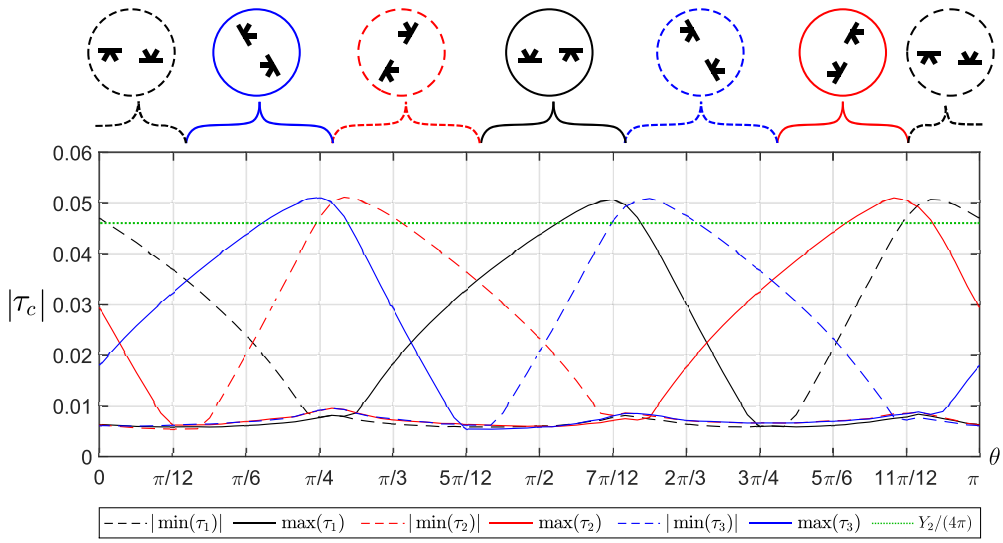

FIG. 5. The value of $|\tau_c|$ at nucleation as a function of the rotation angle θ of the externally imposed stress $\sigma_{ij}^{\text{ext}}(\theta)$. The top row shows the type of dislocation dipole that nucleates. The resolved stress along the slip plane with the largest value determines the type of dislocation dipole to nucleate.

dimensions and behaves near a nucleation event. Here we derive the incompatibility field from the ψ density field corresponding to a bcc lattice in three dimensions and visualize it for a dislocation that is seeded into an otherwise perfect crystal. Since the incompatibility field is determined by the topology of the system, it accurately locates the dislocation strings and provides a powerful tool to visualize mixed edge/screw dislocation loops.

For a suitable range of parameters $\bar{\psi}$ and r, the equilibrium state that minimizes the free energy functional in Eq. (1) is given by a bcc lattice in three dimensions. The corresponding reciprocal lattice vectors lie on a fcc lattice with a lattice constant of unity. We choose as parameter values $\bar{\psi} = -0.371$, $r = -0.4$ for the results presented below. The amplitude of the reciprocal modes in equilibrium is $A_0 = -\frac{2}{15}\bar{\psi} + \frac{1}{15}\sqrt{-5r - 11\bar{\psi}} = 0.2139$ [31]. The orientation of the lattice is chosen by defining the following set of reciprocal lattice vectors of unit length: $\mathbf{q}_1 = [1, 1, 0]/\sqrt{2}$, $\mathbf{q}_2 = [1, 0, 1]/\sqrt{2}$, $\mathbf{q}_3 = [0, 1, 1]/\sqrt{2}$, $\mathbf{q}_4 = \mathbf{q}_1 - \mathbf{q}_3$, $\mathbf{q}_5 = \mathbf{q}_2 - \mathbf{q}_3$, $\mathbf{q}_6 = \mathbf{q}_1 - \mathbf{q}_2$. A cubic computational domain is considered with $30 \times 30 \times 30$ bcc unit cells of length $a_0 = 2\pi$ with grid spacings $\Delta x = \Delta y = \Delta z = a_0/4$.

We first examine a configuration with two dislocation lines added to the phase field by multiplying the initially constant amplitudes $A_{\mathbf{q}_n}$ of the PFC by phase factors $e^{s_n i\theta}$ corresponding to (i) a pure edge dislocation with Burgers vector $\mathbf{b}_1 = \mathbf{e}_x$ and constant tangent line $\mathbf{l}_1 = \mathbf{e}_z$ at $[x_1, y_1] = [20a_0, 15a_0]$ and (ii) a pure edge dislocation with Burgers vector $\mathbf{b}_2 = -\mathbf{e}_x$ and constant tangent line $\mathbf{l}_1 = \mathbf{e}_z$ at $[x_1, y_1] = [10a_0, 15a_0]$. Here θ is the angle in the xy plane relative to the x plane, and s_n is the charge of the dislocation, calculated as in Ref. [20]. The PFC is subsequently prepared, in the one-mode approximation, as $\psi = \psi_0 + \sum_{n=1}^{6}[A_{\mathbf{q}_n}(\mathbf{r})e^{i\mathbf{q}_n\cdot\mathbf{r}} + \text{c.c.}]$ and is allowed to evolve diffusively for few time steps to regularize the dislocation core. The stress tensor is calculated according to Eq. (2), and the strain e_{ij}^{ψ} is found by inverting the stress tensor according to linear elasticity, using the (anisotropic) elastic constants of the bcc lattice given in Ref. [31].

The incompatibility is now a rank-2 tensor with components given by $\eta_{ab}^{\psi} = \epsilon_{aci}\epsilon_{bdj}\partial_{cd}e_{ij}^{\psi}$ [22]. Figure 6(a) shows 2D slices of the PFC after relaxation, with the complex amplitude $A_{\mathbf{q}_1}$ determined by amplitude demodulation of the phase field [23] in Fig. 6(b) and the largest component η_{zz}^{ψ} of the incompatibility tensor in Fig. 6(c). Figure 6 demonstrates how the core of the dislocation lines becomes zeros of the complex amplitudes, with a phase discontinuity of 2π going around a dislocation line. The incompatibility tensor in terms of the dislocation density tensor α_{ij} is given by $\eta_{ik} = (\epsilon_{ipl}\partial_p\alpha_{kl} + \epsilon_{kpl}\partial_p\alpha_{il})$ [32]. For a straight dislocation line with Burgers vector $\mathbf{b} = a_0\mathbf{e}_x$ and tangential vector $\mathbf{l} = \mathbf{e}_z$ [as illustrated in Fig. 6(b) by black lines], the dislocation density tensor is given by its only nonzero component α_{zx}, which gives $\eta_{xx} = \eta_{yy} = \eta_{xy} = \eta_{xz} = \eta_{yz} = 0$ and $\eta_{zz} = -\partial_y\alpha_{zx}$, which is shown in Fig. 6(c). Thus, in this case, $-\eta_{zz}$ is the y component of the gradient of the dislocation density, which explains its dipole structure. The spatial extent of η_{zz} around the dislocation line gives a measure of the spatial smoothing of the dislocation core [27]. This configuration is the straightforward extension of the 2D edge dislocations of Fig. 1(b) to three dimensions. This explains the similarity between the 2D slice of Fig. 6(c) to Fig. 2(b).

In order to demonstrate the intrinsic capability of the phase field and its associated incompatibility field to identify dislocations of mixed edge/screw character, we prepare an initial configuration with a dislocation loop. The Burgers vector of the dislocation line is constant and equal to $a_0\mathbf{e}_x$, while the tangent vector $\mathbf{l}$ rotates in the xy plane. Since $\mathbf{l}$ switches between being parallel to $\mathbf{b}$ and perpendicular, this leads to a mixed edge/screw dislocation. Figure 7(a) shows 2D slices of the PFC, including the defect after relaxation, and the amplitude $A_{\mathbf{q}_1}$ of the first reciprocal lattice vector is shown in Fig. 7(b). For an ideal dislocation loop with Burgers vector $\mathbf{b} = a_0\mathbf{e}_x$

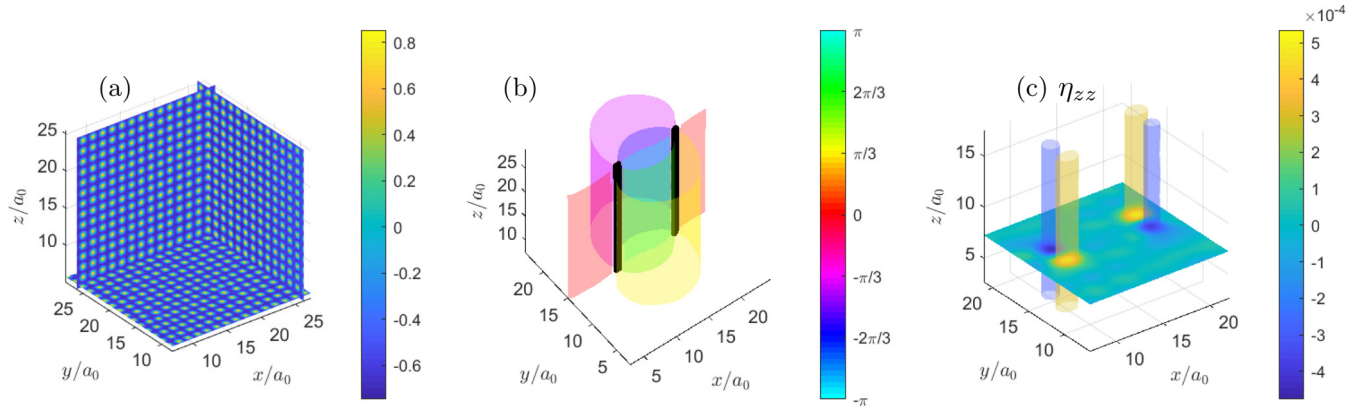

FIG. 6. (a) Two-dimensional slices of the field ψ showing edge dislocations at $[x, y] = [10a_0, 15a_0]$ and $[x, y] = [20a_0, 15a_0]$. (b) The amplitude A_1 of the two dislocation lines in the PFC model. The black subvolume indicates the zeros of the amplitudes and thus the position of the dislocation lines, while the color map gives the complex argument. (c) The η^{ψ}_{zz} component of the incompatibility of dislocation lines in the PFC model. The other components of the incompatibility tensor are small relative to this component (see text).

along the dislocation loop purely in the xy plane, we obtain only a contribution to the dislocation density tensor from α_{ix} with $i \neq z$. To see how the incompatibility field calculated from ψ captures the nature of the defects, consider the portion of the dislocation loop at $\mathbf{r} = [5, 15, 15]$ [red dot in Fig. 7(c)]. Here we have $\mathbf{l} = -\mathbf{e}_y$, which gives α_{yx} as the nonzero com-

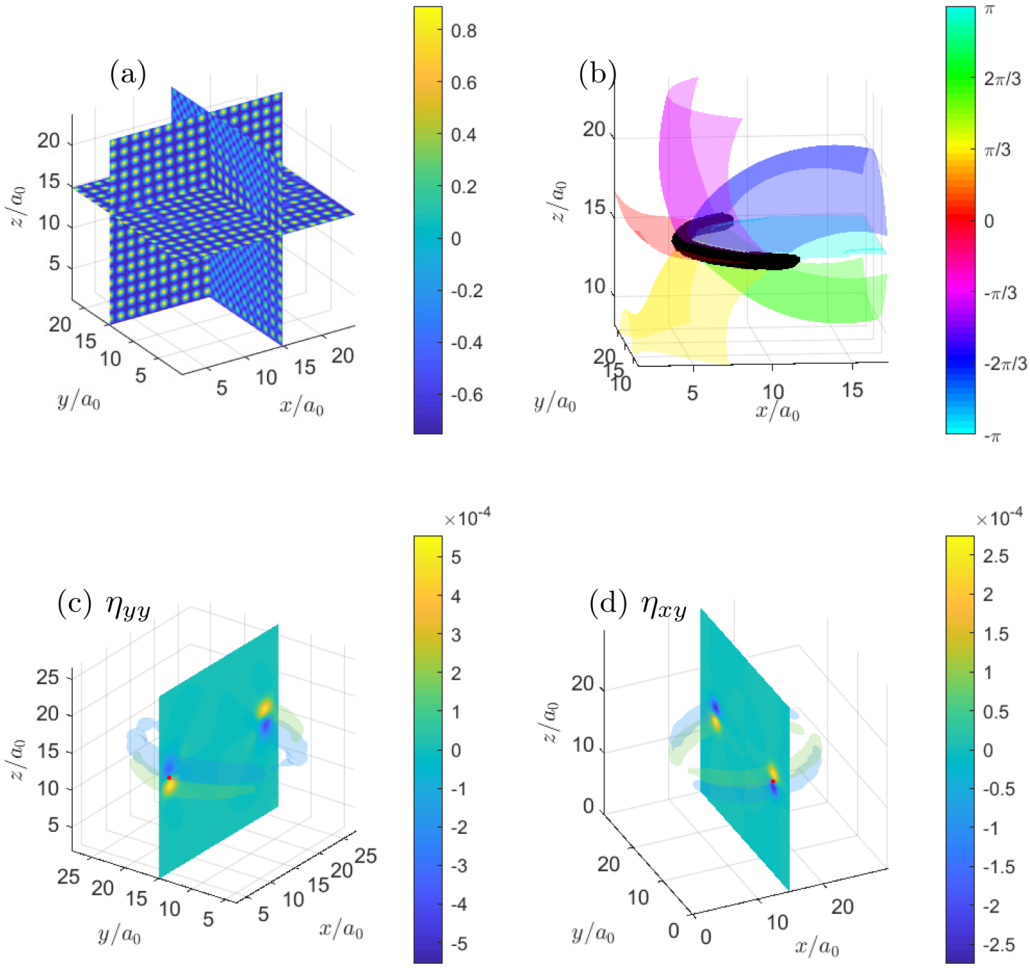

FIG. 7. (a) Two-dimensional slices of the field ψ showing the mixed types of dislocations that appear for a dislocation loop. (b) The amplitude A_1 of the dislocation loop in the PFC model. The black subvolume indicates the zeros of the amplitudes and thus the position of the dislocation lines, while the color map gives the argument. (c) and (d) Two components of the incompatibility tensor η^{ψ}_{ij}. The red dots indicate positions at which the incompatibility field assumes a dipole structure similar to that of Fig. 6(c) as explained in the text.

ponent of the dislocation density tensor. We get $\eta_{yy} = \partial_z \alpha_{yx}$, the z component of the gradient of the dislocation density, and an identical dipole structure as in Fig. 6(c) appears, this time in the z direction. Similarly, at $\mathbf{r} = [15, 5, 15]$ [red dot in Fig. 7(d)], the nonzero component of the dislocation density tensor is α_{xx}, with which $\eta_{xy} = \partial_z \alpha_{xx}/2$, and we recover the dipole structure of Figs. 6(c) and 7(c), its magnitude halved due to the factor of $1/2$ in η_{xy}.

We have exemplified here how the phase field ψ and its associated incompatibility tensor can correctly describe any dislocation string or loop in a given bcc lattice. In further studies, this formalism can be further generalized to other lattice symmetries and also coupled with the evolution of the ψ field to study the dynamics and nucleation of dislocation strings.

VI. CONCLUSION

We have shown for the case of a 2D hexagonal lattice that the incompatibility field η^{ψ} derived from the phase field is a very sensitive diagnostic of the nucleation of a dislocation dipole and that it signals the nucleation event prior to the formation of a stable topological dipole. The symmetry of the field η^{ψ} prior to nucleation also gives the direction of the Burgers vectors of the defect pair about to nucleate. By examining the distribution of the resolved stress for a hexagonal lattice, we have also found it to be a good indicator of nucleation. Furthermore, a balance between the Peach-Koehler force on either one of the defects of the dipole and their mutual elastic interaction force allows a prediction of the resolved critical stress at nucleation that agrees well with the numerical results.

While our results serve to extend those of macroscopic plasticity by allowing the direct observation of the incompatibility field and its evolution under an applied stress, the conclusion that a Schimd-like criterion identifies the nucleation event is in contrast to several existing molecular dynamics simulations. Some of these simulations show that the resolved stress does not predict the location or type of dislocations to nucleate. Instead, it is generally observed that the nominal extent of the nucleation region is very large, with a complex network of stacking faults, partial dislocations, and other significant sources of lattice distortion. These results would imply that the nucleation path in three-dimensional (3D) configuration space can be much more complex than in our 2D configuration, with possibly multiple competing trajectories that depend on details such as boundaries or applied stress protocols.

Our results indicate that the phase-field crystal model provides adequate control over configurations and applied stresses around the nucleation threshold and hence is a suitable platform for testing nucleation criteria. The model offers the necessary separation between length scales, eliminates fluctuations of thermal origin, and allows the computation of internally generated stress that contributes to lattice incompatibility and, ultimately, to nucleation. This bypasses the need for extensive averaging of molecular dynamics trajectories along paths in configuration space in which fluctuations are very small.

Finally, we presented results for a 3D bcc lattice to show that the phase field can be used to describe dislocations in this lattice and that it offers the possibility of computing the incompatibility tensor directly from the phase field for arbitrary, nonequilibrium configurations.

ACKNOWLEDGMENTS

We thank A. Acharya, K. Olsen, and J. Rønning for many stimulating discussions. The research of J.V. was supported by the National Science Foundation, Grant No. DMR-1838977. L.A. acknowledges support from the Kavli Institute for Theoretical Physics through the National Science Foundation under Grant No. NSF PHY-1748958.

[1] J. S. Langer, Ann. Phys. (NY) **54**, 258 (1969).
[2] J. Gunton, M. San Miguel, and P. Sahni, in *Kinetics of First Order Phase Transitions*, edited by C. Domb and J. Lebowitz, Phase Transitions and Critical Phenomena Vol. 8 (Academic, London, 1983).
[3] A.-C. Davis and R. H. Brandenberger, *Formation and Interactions of Topological Defects*, NATO Advanced Studies Institute, Series B: Physics (Plenum, New York, 1995), Vol. 349.
[4] J. Friedel, in *Dislocations in Solids*, edited by F. R. N. Nabarro (North-Holland, Amsterdam, 1979), Vol. 1, pp. 1–32.
[5] R. Phillips, *Crystals, Defects and Microstructures: Modeling Across Scales* (Cambridge University Press, 2001).
[6] J. Li, K. J. Van Vliet, T. Zhu, S. Yip, and S. Suresh, Nature (London) **418**, 307 (2002).
[7] R. E. Miller and A. Acharya, J. Mech. Phys. Solids **52**, 1507 (2004).
[8] A. Garg, A. Acharya, and C. E. Maloney, J. Mech. Phys. Solids **75**, 76 (2015).
[9] C. L. Kelchner, S. J. Plimpton, and J. C. Hamilton, Phys. Rev. B **58**, 11085 (1998).
[10] T. Zhu, J. Li, A. Samanta, A. Leach, and K. Gall, Phys. Rev. Lett. **100**, 025502 (2008).
[11] X. Li, Y. Wei, L. Lu, K. Lu, and H. Gao, Nature (London) **464**, 877 (2010).
[12] K. R. Elder, M. Katakowski, M. Haataja, and M. Grant, Phys. Rev. Lett. **88**, 245701 (2002).
[13] H. Emmerich, H. Löwen, R. Wittkowski, T. Gruhn, G. Tóth, G. Tegze, and L. Gránásy, Adv. Phys. **61**, 665 (2012).
[14] J. R. Rice, J. Mech. Phys. Solids **40**, 239 (1992).
[15] J. Li, T. Zhu, S. Yip, K. J. Van Vliet, and S. Suresh, Mater. Sci. Eng., A **365**, 25 (2004).
[16] R. E. Miller and D. Rodney, J. Mech. Phys. Solids **56**, 1203 (2008).
[17] A. Garg and C. E. Maloney, J. Appl. Mech. **83**, 121006 (2016).
[18] M. Duesbery and V. Vitek, Acta Mater. **46**, 1481 (1998).

[19] K. R. Elder, N. Provatas, J. Berry, P. Stefanovic, and M. Grant, Phys. Rev. B **75**, 064107 (2007).
[20] A. Skaugen, L. Angheluta, and J. Viñals, Phys. Rev. B **97**, 054113 (2018).
[21] This version of the microscopic stress tensor is slightly different than that in [20], but it has the same divergence. Therefore, they are physically equivalent.
[22] E. Kröner, in *Physics of Defects*, edited by R. Balian, M. Kléman, and J.-P. Poirier, Les Houches, Session 35 (North-Holland, Amsterdam, 1981), pp. 215–315.
[23] A. Skaugen, L. Angheluta, and J. Viñals, Phys. Rev. Lett. **121**, 255501 (2018).
[24] A. Acharya and J. Viñals, Phys. Rev. B **102**, 064109 (2020).
[25] V. Heinonen, Ph.D. thesis, Aalto University, 2016.
[26] S. M. Cox and P. C. Matthews, J. Comput. Phys. **176**, 430 (2002).
[27] M. Salvalaglio, L. Angheluta, Z.-F. Huang, A. Voigt, K. R. Elder, and J. Viñals, J. Mech. Phys. Solids **137**, 103856 (2020).
[28] See Supplemental Material at http://link.aps.org/supplemental/10.1103/PhysRevB.103.014107 for a video animation of the nucleation event sequence.
[29] P. M. Chaikin and T. C. Lubensky, *Principles of Condensed Matter Physics* (Cambridge University Press, Cambridge, 1995).
[30] B. Perreault, J. Viñals, and J. M. Rickman, Phys. Rev. B **93**, 014107 (2016).
[31] K.-A. Wu and A. Karma, Phys. Rev. B **76**, 184107 (2007).
[32] A. M. Kosevich, in *Dislocations in Solids*, edited by F. R. N. Nabarro (North-Holland, Amsterdam, 1979), Vol. 1, pp. 33–141.